Simulation-guided photothermal therapy using MRI-traceable iron oxide-gold nanoparticle

Jaber Beik[a], Mohamadreza Asadi[a], Samideh Khoei[a], Sophie Laurent[b], Ziaeddin Abed[a], Mehri Mirrahimi[a], Ali Farashahi[a], Reza Hashemian[c], Habib Ghaznavi[d,*], Ali Shakeri-Zadeh[a,*]

[a] Medical Physics Department, School of Medicine, Iran University of Medical Sciences (IUMS), Tehran, Iran
[b] General, Organic and Biomedical Chemistry, NMR and Molecular Imaging Laboratory, University of Mons, Mons, Belgium
[c] US oncology Inc., Cincinnati, OH, USA
[d] Zahedan University of Medical Sciences (ZaUMS), Zahedan, Iran

ARTICLE INFO

ABSTRACT

Despite the immense benefits of nanoparticle-assisted photothermal therapy (NPTT) in cancer treatment, the limited method and device for detecting temperature during heat operation significantly hinder its overall progress. Development of a pre-treatment planning tool for prediction of temperature distribution would greatly improve the accuracy and safety of heat delivery during NPTT. Reliable simulation of NPTT highly relies on accurate geometrical model description of tumor and determining the spatial location of nanoparticles within the tissue. The aim of this study is to develop a computational modeling method for simulation of NPTT by exploiting the theranostic potential of iron oxide-gold hybrid nanoparticles (IO@Au) that enable NPTT under magnetic resonance imaging (MRI) guidance. To this end, CT26 colon tumor-bearing mice were injected with IO@Au nanohybrid and underwent MR imaging. The geometrical model description of tumor and nanoparticle distribution map were obtained from MR image of the tumor and involved in finite element simulation of heat transfer process. The experimental measurement of tumor temperature confirmed the validity of the model to predict temperature distribution. The constructed model can help to predict temperature distribution during NPTT and then allows to optimize the heating protocol by adjusting the treatment parameters prior to the actual treatment operation.

1. Introduction

The high mortality rate of cancer worldwide reflects the inefficiency of the current treatment modalities to achieve a satisfactory therapeutic outcome. As a complementary treatment modality, hyperthermia at mild temperatures (41–45 °C) has been widely utilized in order to enhance the cytotoxic effects of chemotherapy and radiation therapy [1,2]. Furthermore, the separate application of hyperthermia at lethal thermal range (> 47 °C) has successfully resulted in direct ablation of tumor cells in various cancer cases [3,4]. A recent progress in nanomedicine has been the introduction of thermo-responsive nanoparticles capable of converting the energy originated form hyperthermia source into heat, thereby confining heat generation to the tumor site while minimizing heat exposure to the collateral tissues [5,6].

Owing to their unique thermo-physical properties, inherent bioinertness and facile synthesis, gold nanoparticles (AuNPs) have been suggested as one of the leading nanomaterials for nanoparticle-assisted photothermal therapy (NPTT) [7,8]. In this method, the incident laser beam is absorbed following interaction with AuNPs, resulting in localized temperature elevation. The successful application of NPTT in real condition requires the accurate prediction of temperature distribution and its resultant thermal damages. Pre-treatment planning of NPTT using computational simulation can be helpful to optimize this strategy through adjusting various treatment parameters including laser irradiation condition and nanoparticles concentration before the actual heating session [9]. This is an imperative prerequisite, in order to ensure if the administrated NPTT regimen would apply a lethal thermal dose to the whole tumor volume while preserving the surrounding normal tissues from unwanted thermal damages [10].

To achieve an accurate simulation of NPTT, the original shape and size of tumor, as well as the nanoparticle distribution map within the tumor need to be determined and included in numerical modeling process. Recent progress in nanomedicine has led to development of multifunctional theranostic nanoparticles through integrating diagnostic and

therapeutic potentials into a single platform for simultaneous monitoring of treatment process [11,12]. The core-shell structure of iron oxide-gold hybrid nanoparticles (IO@Au) has gained great attention in this area [13,14]. The magnetic core of IO@Au allows to detect its spatial location via magnetic resonance imaging (MRI). It also establishes a magnetic targeting strategy by which nanoparticles can be targeted to the tumor under an external magnetic field. Moreover, the gold layer can simultaneously enable NPTT upon laser irradiation. Compared to the spherical AuNPs which have a plasmon resonance peak at visible wavelength range, the core-shell nanostructure of IO@Au offers an optical resonance which can be tuned to the near-infrared (NIR) region. This is considered as an optical therapeutic window for deeper penetration of light into the body due to its minimal absorption by the biological absorbers (e.g., hemoglobin and melanin) [15].

The present study attempts to develop an individualized pre-treatment planning strategy for NPTT based on MR image of the tumor. To this end, colon tumor-bearing mice were injected with IO@Au nanoparticles and imaged through MRI. The actual tumor geometry and nanoparticle distribution map were obtained from MR images of the mice and exported into a finite element simulation software to predict temperature distribution. The model was validated in experiment through measuring the temperature variations of the tumor under laser irradiation. Moreover, the resulting thermal damage of the tumor was assessed through histological study and follow-up of tumor growth. Fig. 1 shows the work flow of the present study.

2. Materials and Methods

2.1. Materials

Iron (II) chloride tetrahydrate (> 99%), iron (III) chloride hexahydrate (> 99%), ammonia (32%), hydrochloric acid (HCl), Nitric acid (HNO3), N-hydroxysuccinimide, dicyclohexylcarbodiimide were purchased from Merck (Darmstadt, Germany) for the synthesize of nanoparticles. Dubelco's Modification of Eagle's Medium (DMEM) was purchased from GIBCO (Invitrogen, Germany). Fetal bovine serum (FBS) was purchased from BioSera Ltd. (Ringmer, United Kingdom). Trypsin-ethylenediaminetetraacetic acid (EDTA) and penicillin-streptomycin solution were purchased from Sigma–Aldrich Corp. (St Louis, MO, USA). All the materials were used for cell culture.

2.2. Synthesis and Characterization of Nanoparticles

Synthesis and full characterization of nanoparticles were reported in our previous paper [16]. Transmission electron microscopy (TEM) revealed that IO@Au has a magnetic core of 20 nm diameter, and Au shell with ~3 nm thickness uniformly covers the magnetic core. Hydrodynamic diameter of nanoparticles measured by dynamic light scattering (DLS) was ~33 nm. Moreover, nanoparticles displayed a characteristic surface plasmon absorption at 584 nm. The absorption of IO@Au at 808 nm (the laser wavelength used in this study) is about 80% of its maximum absorption at 584 nm. Further information can be found in the mentioned reference.

2.3. Tumor Induction

CT26 cell line derived from mouse colon adenocarcinoma and male BALB/c mice (5–8 weeks old and weighing 20–25 g) were obtained from Pasteur Institute of Iran. Cells were cultured in RPMI 1640 medium with 10% FBS, 100 units/ml penicillin, and 100 μg/ml streptomycin at 37 °C in 5% CO_2. Cells were harvested by trypsinizing cultures with 1 mM EDTA/0.25% Trypsin (*w/v*) in PBS. After three passages, 2×10^6 CT26 cells suspended in 200 μl RPMI 1640 solution were injected subcutaneously on the right flank of BALB/c mice. All the animal experiments were conducted in accordance with guidelines established by the Institutional Animal Care Committee.

2.4. Determination of Nanoparticles Distribution by MRI

As mentioned earlier, due to its magnetic core, IO@Au can be tracked via MRI and also be targeted toward the tumor by means of magnetic field. To test these potentials simultaneously, tumor-bearing mice were intravenously (IV) injected with IO@Au and the tumor localization of nanoparticles in the presence and absence of magnetic drug targeting (MDT) was explored via MRI. For IV injection alone, 200 μl of nanoparticles solution ([Au]: 20 mM, [Fe]: 2 mM) was injected through the tail vein and the mice were imaged after 24 h. For MDT group, subsequent to IV injection of nanoparticles (with the same concentration) a magnet (magnetic field strength of 0.4 Tesla) was placed on the tumor for 3 h in order to accumulate nanoparticles into the tumor, and thereafter mice were imaged. Moreover, mice without nanoparticles injection were imaged to be used as control. Three mice were used in each group. MRI study was performed by using Philips superconductor clinical MR system (1.5 T) with the following acquisition parameters: T2* weighted gradient echo, TR: 250 ms, TE: 11 ms, FA: 25, slice thickness: 2 mm, FOV: 150 mm, matrix size: 304 × 213.

Finally, inductively coupled plasma mass spectrometry (ICP-MS, ELAN DRC-e spectrometer; PerkinElmer SCIEX, Concord, Ontario, Canada) was performed to determine the Au content of tumors. To this end, mice in IV injection and IV injection + MDT groups were euthanized at 24 h and 3 h post-injection, respectively, and the tumors were collected for ICP-MS analysis.

2.5. Geometrical Model Generation

MR images were processed in MATLAB prior to being imported into finite element simulation software for heat transfer modeling. Images were segmented for quantification of MR signals before and after injection. Then, a single fixed threshold signal intensity was set manually based on the difference in the signal intensity of the tumor before and after injection of nanoparticles in order to distinguish nanoparticles from the tumor tissue in MATLAB and delineate nanoparticle
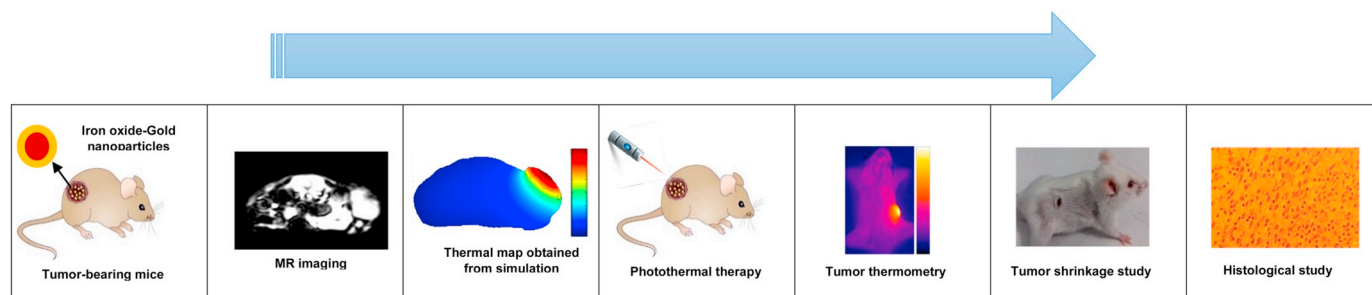

Fig. 1. Schematic workflow diagram of the present study.

distribution contour. The average pixel index number of tumor without nanoparticles injection was ranged from 235–245. Since the presence of nanoparticles resulted in darkening of MR images (hypointense area), a region with the pixel index number < 235 was considered as the location of nanoparticles. Additionally, MR images were converted into color maps to better indicate how nanoparticles change the signal intensity of MR images. Accordingly, every pixel with an intensity value above the threshold (235) was shown as yellow and considered the absence of nanoparticles, whereas every pixel with an intensity value below the threshold was associated to the spatial location of nanoparticles. Subsequently, a gradient edge detection filter was applied to identify mice body contour. Then, the geometry model was imported into COMSOL Multiphysics® modeling software (version 5.2) for heat transfer simulation [17].

2.6. Computational Modeling of Temperature Distribution

Firstly, light distribution inside the mouse body was calculated using the radiative transport theory [18], and secondly, the Pennes bioheat transfer equation was applied to determine temperature distribution within the tissue.

2.6.1. Laser-heating Model

When light propagates through the tissue, it will undergo absorption and scattering depending upon the absorption (μ_a) and scattering (μ_s) coefficients of the tissue. In the case of soft tissues where the scattering coefficient is much larger than the absorption coefficient ($\mu_s \gg \mu_a$), an approximation to the radiative transport equation can be applied. Therefore, the light diffusion in the tissue can be determined by the following approximation [19]:

$$- D\nabla^2\varphi(r,t) + \mu_a\varphi(r,t) = s(r,t) \tag{1}$$

where $\varphi(r,t)$ is the light fluence rate (W/m^2), $s(r,t)$ is the source term (W/m^3), t is time (s), r is Cartesian coordinate (m), and D is the diffusion coefficient (m) given by:

$$D = \frac{1}{3(\mu_s' + \mu_a)} \text{ with } \mu_s' = \mu_s(1-g) \tag{2}$$

where μ_s' is the reduced scattering coefficient in tissue and g is the anisotropy factor which is typically chosen as > 0.9 for most tissues, implying that most scattering events result in forwarding motion of photons [20].

When nanoparticles are injected into the tissue, they will alter the overall tissue optical properties and hence the laser fluence. The total absorption (μ_{atot}) and total reduced scattering (μ_{stot}') coefficients of a tissue due nanoparticle inclusion can be obtained as follows [21]:

$$\mu_{atot} = \mu_{at} + \mu_{an}, \mu_{stot} = \mu_{st} + \mu_{sn} \tag{3}$$

where μ_{at} and μ_{st}' are the absorption and reduced scattering coefficients of the tissue, and μ_{an} and μ_{sn} are the absorption and scattering coefficients of nanoparticles. According to Mie theory the absorption and scattering coefficient of nanoparticles can be calculated by the following equations [22]:

$$\mu_{an} = 0.75 f_v \frac{C_{abs}}{\pi a^3}, \mu_{sn} = 0.75 f_v \frac{C_{sct}}{\pi a^3} \tag{4}$$

where C_{abs} and C_{sct} stand for the absorption and scattering cross section respectively, f_v is the volume fraction of the nanoparticles and a represents the nanoparticle radius. Therefore, it is obvious that the inclusion of nanoparticles will consequently increase the total absorption and scattering coefficients of the tissue, which in turn alter the heat generation and thermal distribution.

2.6.2. Bioheat Transfer Model

After determining the laser energy deposition within the tissue following the interaction of incident laser beam and nanoparticles, the Pennes bioheat Eq. (5) was used to measure the resultant temperature distribution [23].

$$\rho c \frac{\partial T(r,t)}{\partial t} = \nabla(k\nabla T(r,t)) + Q_p + Q_m + Q_s \tag{5}$$

where ρ, c and k denote the density, specific heat and thermal conductivity of the tissue. Q_p incorporates the heat gained or lost due to local blood perfusion, calculated as $Q_p = \rho_b c_b \omega_b(T_b - T)$, where ω_b, ρ_b, c_b, and T_b stand for blood parameters including perfusion rate, density, specific heat and temperature, respectively. Q_m is volumetric metabolic heat generation rate, and Q_s is the volumetric heat generated caused by laser irradiation, and can be expressed as [19]:

$$Q_s(r,t) = \mu_a\,\varphi(r,t)\,(W/m^3) \tag{6}$$

To consider heat loss at the boundary between the surface of the mouse body and air due to the convection mechanism, a Neumann boundary condition was applied, given by [19]:

$$- k\frac{\partial T}{\partial n} = h(T_b - T_\infty) \tag{7}$$

where h is the convective transfer coefficient, n is the unit outward normal, T_b and T_∞ are the temperature at the boundary and the ambient temperature of the environment (24 °C), respectively. Table 1 represents the numerical values of the thermal and optical characteristics of the tissue and nanoparticles used for model simulation in this study.

2.7. In Vivo Photothermal Treatment

After MRI examination, tumor-bearing mice were exposed with a continuous-wave 808 nm NIR laser source (Nanobon Company, Tehran, Iran) under the same conditions as considered in computational modeling (1.4 W/cm^2, 15 min). Two additional groups including control (untreated) and laser irradiation alone also served to better demonstrate the photothermal ablation effect of IO@Au. During laser irradiation, the superficial temperature of the tumor was monitored with an infrared (IR) thermal camera (Testo 875–1i, Germany). To determine the antitumor effect of various treatments, as modeled in COMSOL software, the tumor volume changes were monitored until 7 days after treatment. The tumor volume was calculated as: $\frac{\pi}{6} \times$ length $\times$ (width)^2. Five mice were considered in each group.

Table 1
Symbols and values of the parameters considered in this study [24,25].

| Parameter	Value	Parameter	Value
Density, ρ	1052 kg/m^3	Density of blood, ρ_b	1052 kg/m^3
Specific heat, c	3800 J/kg.K	Specific heat of blood, c_b	3800 J/kg.K
Thermal conductivity, k	0.545 W/mK	Blood perfusion, ω_b	0.01 1/s
Convective coefficient, h	10 W/m^2.K	Blood temperature, T_b	37 °C
Power density,	1.4 W/cm^2	Ambient temperature, T_e	24 °C
Absorption coefficient, μ_{at}	0.8 1/cm	Transport scattering coefficient, μ_{st}'	10 1/cm
Absorption coefficient of nanoparticles (IV), μ_{an}	1.85 1/cm	Transport scattering coefficient of nanoparticles (IV), μ_{sn}'	0.11e-2 1/m
Absorption coefficient of nanoparticles (MDT), μ_{an}	2.65 1/cm	Transport scattering coefficient of nanoparticles (MDT), μ_{sn}'	0.16e-2 1/m
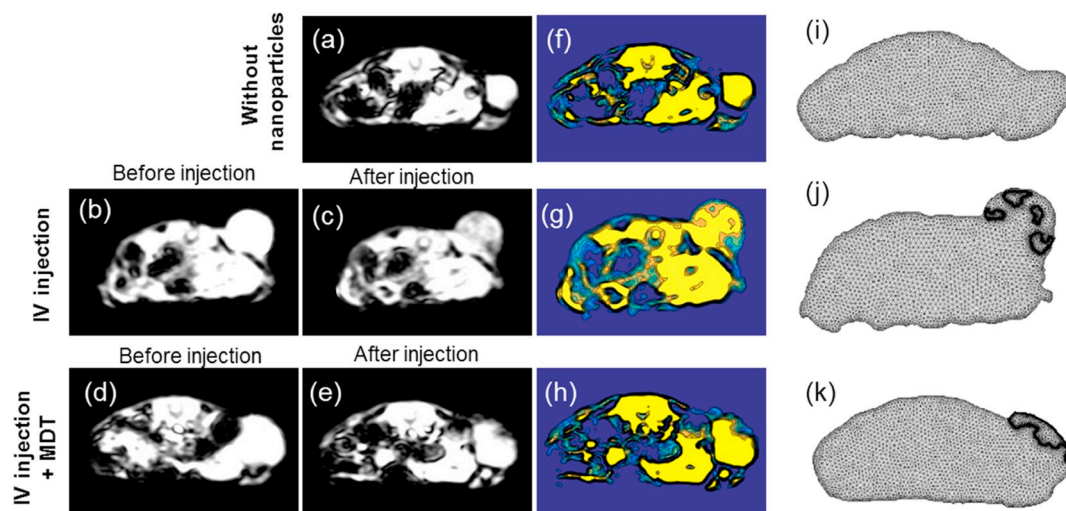
Fig. 2. Geometrical model generation of tumor by MRI. MR images of tumor-bearing mice (a) without nanoparticles, (b-c) before and after IV injection of IO@Au and (d-e) before and after IV injection of IO@Au followed by magnetic targeting. The hypointense area in the MR image indicates the spatial location of nanoparticles. (f–h) The color maps generated from MR images. (i-k) The corresponding image-generated tumor geometries with mesh configuration in COMSOL software. The black bold lines indicate the contour of nanoparticle distribution.

Histological examination of tumor tissue using hematoxylin-eosin (H&E) staining was also performed (48 h post-treatment) to further confirm the antitumor efficacy of various treatments.

2.8. Statistical Methods

Statistical analysis was performed by one-way ANOVA test by using SPSS software (version11). Then, the Tukey test at 95% confidence level was used as a post hoc test for pairwise comparison of means of the treatment groups. Measurement data are mean ± standard deviation (SD). A value of $P < .05$ was considered statistically significant.

3. Results

3.1. Geometrical Model Generation

MRI study was performed for actual description of tumor geometry and nanoparticle distribution map. Fig. 2a indicates a representative MR image of tumor-bearing mice without nanoparticles inclusion, showing the baseline level of soft tissue image contrast. MR image of the mice at 24 h post IV injection of nanoparticles displays several hypointense regions in the tumor that appear as dark spots, indicating the spatial location of nanoparticles (Fig. 2c). In contrast, IV injection of nanoparticles followed by magnetic targeting generated markedly dark regions under the surface of the tumor which is the evidence for the accumulation of nanoparticles (Fig. 2e). This indicates the effective tumor targeting of nanoparticles by means of magnetic field. In addition, the color maps generated from MR images clearly demonstrate the spatial location of nanoparticles (Fig. 2f–h). MR images were then

processed in MATLAB as described in "Section 2.5", and the MR image-generated tumor geometries were imported into COMSOL software for subsequent heat transfer modeling. The geometry model was meshed with non-uniform size and shape grids and finite element simulation was then carried out for each element separately (Fig. 2i–k).

3.2. Heat Transfer Simulation

After preparation of the model geometry, a two-dimensional finite element simulation was conducted to solve the radiative transport equation and then the Pennes bioheat equation for estimation of temperature distribution. The presence of nanoparticles increases the total absorption and scattering coefficients of tissue depending on the nanoparticles content of tissue. The biodistribution analysis of IO@Au using ICP-MS revealed that the Au content of the tumor 24 h post-IV injection of nanoparticles was 6.2 μg. Accordingly, the volume fraction of nanoparticles due to IV injection was calculated to be 2.52×10^{-6}. Likewise, the Au content and the volume fraction of nanoparticles for mice treated with IV injection + MDT were 9.8 μg and 3.6×10^{-6}, respectively. Therefore, magnetic targeting was effective to accumulate nanoparticles in the tumor.

Fig. 3 shows the transversal cross-sections of the mice body with a representative temperature distribution map at the end of 15 min NIR laser irradiation with power density of 1.4 W/cm². The tumor treated with laser alone showed a mild temperature gradient with the maximum temperature of 42.5 °C at the tumor surface. However, the presence of nanoparticles changed the temperature distribution pattern and increased the temperature elevation rate of the tumor. Accordingly, the tumors treated with IV injection of nanoparticles or IV injection +
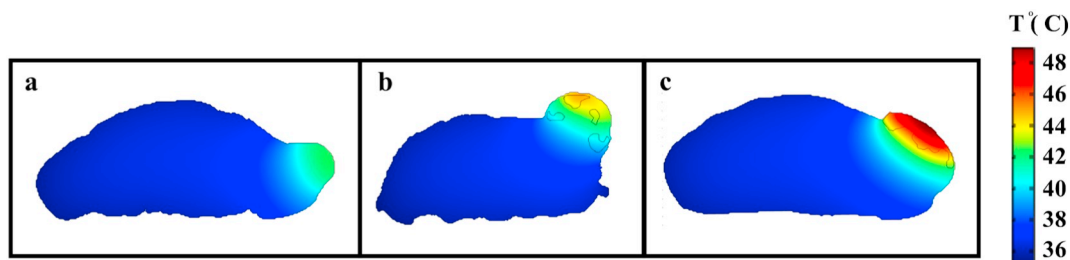

Fig. 3. Simulated temperature distribution map on transversal cross-section of tumor-bearing mice after 15 min NIR irradiation in mice pretreated (a) without IO@Au, (b) with IV injection of IO@Au and (c) with IV injection of IO@Au followed by magnetic targeting.
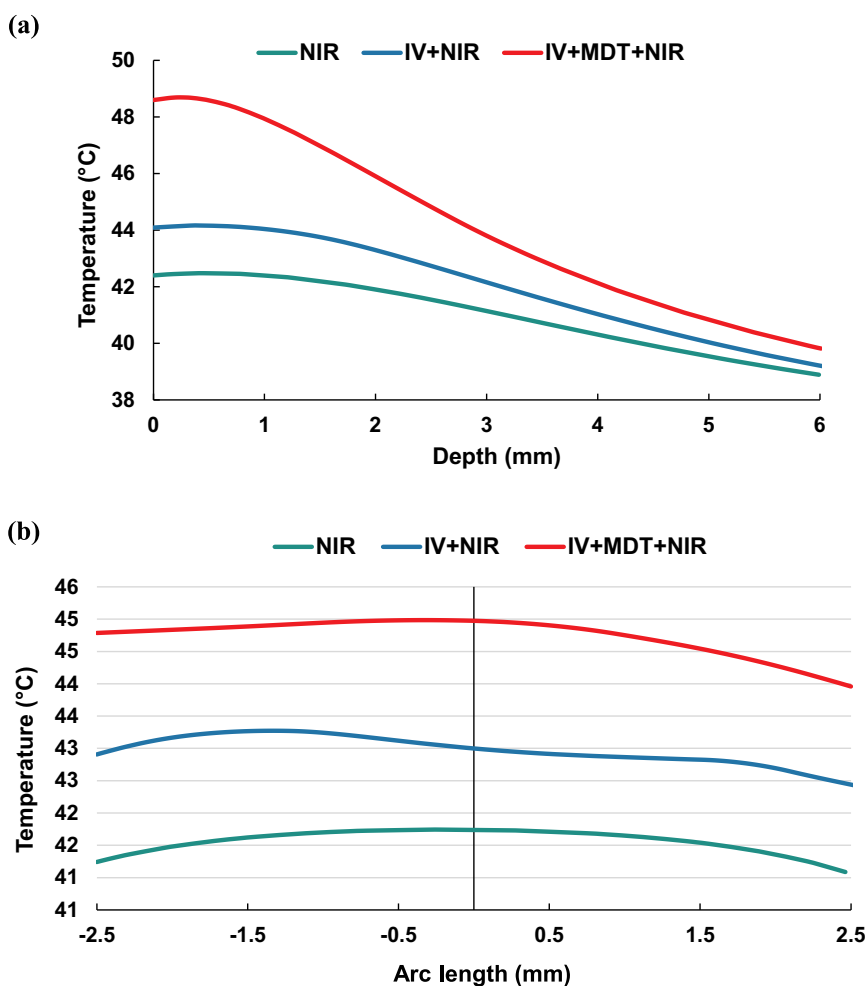
(a)

(b)

Fig. 4. Temperature variation profile of tumor after 15 min NIR irradiation, (a) as a function of depth along the vertical central axis of the tumor, and (b) as a function of radial distance at the fixed depth of 2.5 mm.

MDT exhibited the maximal temperature of 44.8 and 48.6 °C, respectively, after 15 min laser irradiation. Fig. 4a is a detailed graph that indicates the temperature variations as a function of depth along the central axis of the tumor. Obviously, a steeper temperature gradient forms in the tumor treated with IV + MDT + NIR due non-uniformity in nanoparticle distribution and high accumulation of nanoparticles under the tumor surface that limits the heat generation to the superficial region of tumor. Fig. 4b shows the variation of temperature profile as a function of radial distance at the fixed depth of 2.5 mm. As shown in this figure, the difference between the minimum and maximum temperature along the tumor path becomes more prominent when nanoparticles are included in the tumor, indicating additional non-uniformity in temperature distribution due to the presence of nanoparticles.

3.3. Experimental Validation

To evaluate the prediction power of the constructed model, the numerical simulation needs to be validated in experiment under the exactly similar conditions. To this end, the superficial temperature variation of the tumor obtained from thermal camera, as a representative, was compared with simulation. Generally, application of heat to tumor causes a transient temperature rise followed by a steady-state temperature. As shown in Fig. 5, there is an unsatisfactory difference between the theoretical predictions and practical observations in the transient temperature phase, especially in case nanoparticles are included. However, this difference starts to decrease when temperature

reaches to a steady-state. After 15 min laser irradiation, the predicted temperature of the tumor without nanoparticles was quite in agreement with the measured temperature. For tumor treated with IV + NIR and IV + MDT + NIR the mean temperature deviation between the simulation and experiment was 0.7 and 0.2 °C, respectively. These results suggest the satisfactory performance of the constructed model to predict steady-state temperature distribution in NPTT.

3.4. In Vivo Antitumor Assessment

To recognize the extent of thermal damage induced by various heating regimens as simulated before, the tumor shrinkage and pathological condition of tumor tissue were evaluated (Fig. 6). The tumor rapidly grew in control group and showed an average volume of 1400 mm^3 on day 7 after treatment start. Compared to control group, NIR irradiation alone inhibited the tumor growth to some extent and the tumor volume was found to be 735 mm^3. The mice treated with IV injection of nanoparticles followed by NIR irradiation exhibited a significant tumor growth inhibition, showing the tumor volume of 390 mm^3. In sharp contrast, magnetically targeting of nanoparticles plus NIR irradiation remarkably suppressed the tumor growth and reduced the tumor volume to < 50 mm^3, which was smaller than that of initial tumor (~150 mm^3). Representative photographs of the mice clearly compares the tumor shrinkage ability of the treatments (Fig. 6b). Accordingly, the enhanced accumulation of nanoparticles due to magnetic targeting which was confirmed by MRI study and in vivo thermometry resulted in dramatic shrinkage of tumor mass and left a
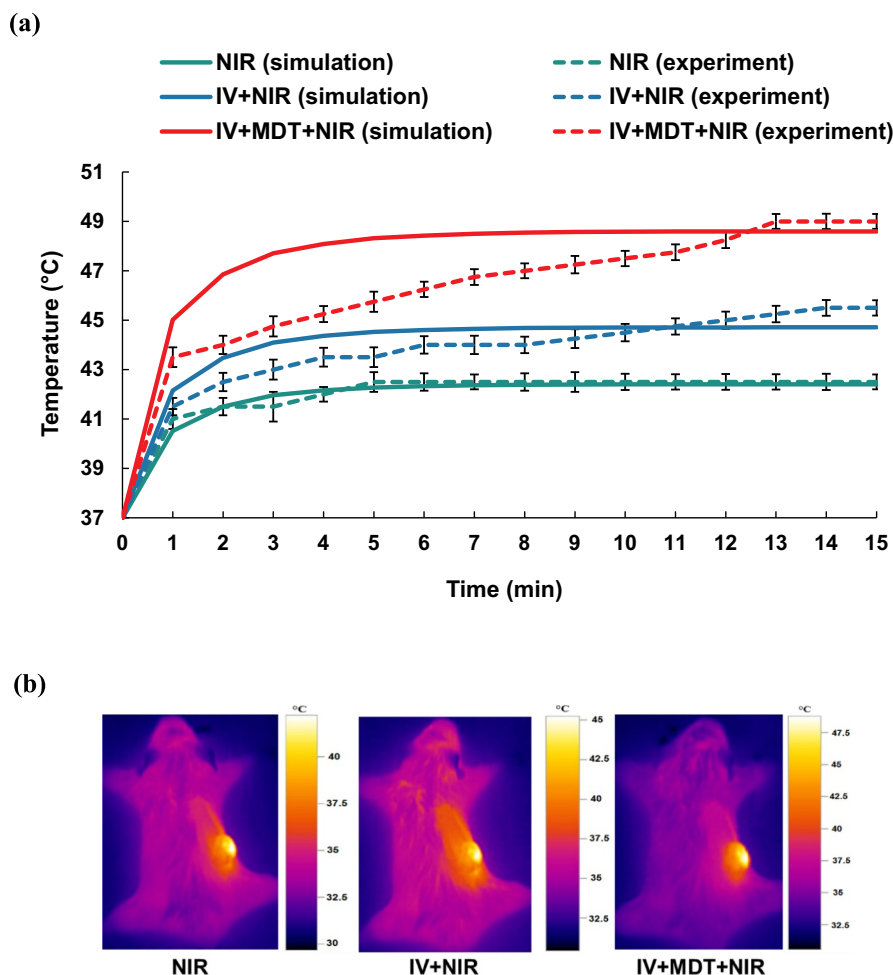
(a)

(b)

Fig. 5. (a) Comparison of the predicted and measured temperature rise profile of the tumor during NIR irradiation (Error bar indicates standard deviation for five mice in each group). (b) The representative infrared thermal image of the tumor bearing mice after 15 min NIR irradiation (808 nm, 1.4 W/cm^2).

black scar at the tumor site, indicating the evidence of extensive necrosis. Histological examination of tumor tissue of mice subjected to NIR and IV + NIR revealed a decreased cell density and evidence of cell necrosis compared to control group. On the contrary, an extensive area of necrotic cells can be clearly seen in the tumor section of mice treated with IV + MDT + NIR (Fig. 6c).

4. Discussion

Chemotherapy and radiotherapy have shown remarkable improvement at elevated temperatures because of the several physiology-related mechanisms that increase the susceptibility of tumor cells to anticancer drugs and ionizing radiation. Accordingly, the concurrent applications of chemotherapy and hyperthermia or radiotherapy and hyperthermia have been a well-established treatment paradigm in clinical oncology for cancer management [26]. Despite the outstanding therapeutic benefits, hyperthermia still faces serious problems in practice that hamper its extensive clinical use. Understanding the temperature of tissue during hyperthermia operation is a major challenge in current clinical practice. Invasive thermometry using thermocouples only provides sporadic and unreliable temperature information at limited locations in the body and is also accompanied with the risk of complications and metastasis [27]. On the other hand, non-invasive thermometry using MRI that enables a real time temperature monitoring strategy is limited by several problems, such as costly process, interference with hyperthermia device, limited availability, insufficient accuracy and not applicable for all tissue types [28].

Pre-treatment planning of hyperthermia using computational simulation offers important advantages which are necessary to promote the clinical utility of hyperthermia. Computational simulation of hyperthermia is able to predict the 3D temperature distribution map within the body which is required to ensure if the whole tumor volume reaches to the target temperature. Therefore, simulation of hyperthermia can help to prevent either unheated regions within the tumor which may contribute to recurrence, or hot spots which may cause unwanted thermal damages to the surrounding normal tissues. This could be realized by modifying the treatment parameters before the actual heating operation in any individual condition [9,29].

Currently, several treatment planning tools have been developed for prediction of temperature distribution during radiofrequency- and microwave-induced hyperthermia [30,31]. However, no treatment planning tool has been yet validated to be able to predict temperature during NPTT. In this case, nanoparticles act as a source of heat and generate localized heat subsequent to interaction with laser light field. Therefore, determining the precise location of nanoparticles in the body is a primary requirement for accurate prediction of temperature distribution. Unfortunately, nanoparticles distribution in the tumor is not possible to predict due to heterogeneous tumor geometries, differences in tumor porosity that affects tumor penetration of nanoparticles, and the random interaction of nanoparticles with cell membrane [32]. Recent efforts for computational modeling of NPTT have been based on simple description of tumor geometry and simple patterns of nanoparticles distribution such as a uniform or a Gaussian distribution [33,34]. Therefore, taking into consideration the actual tumor
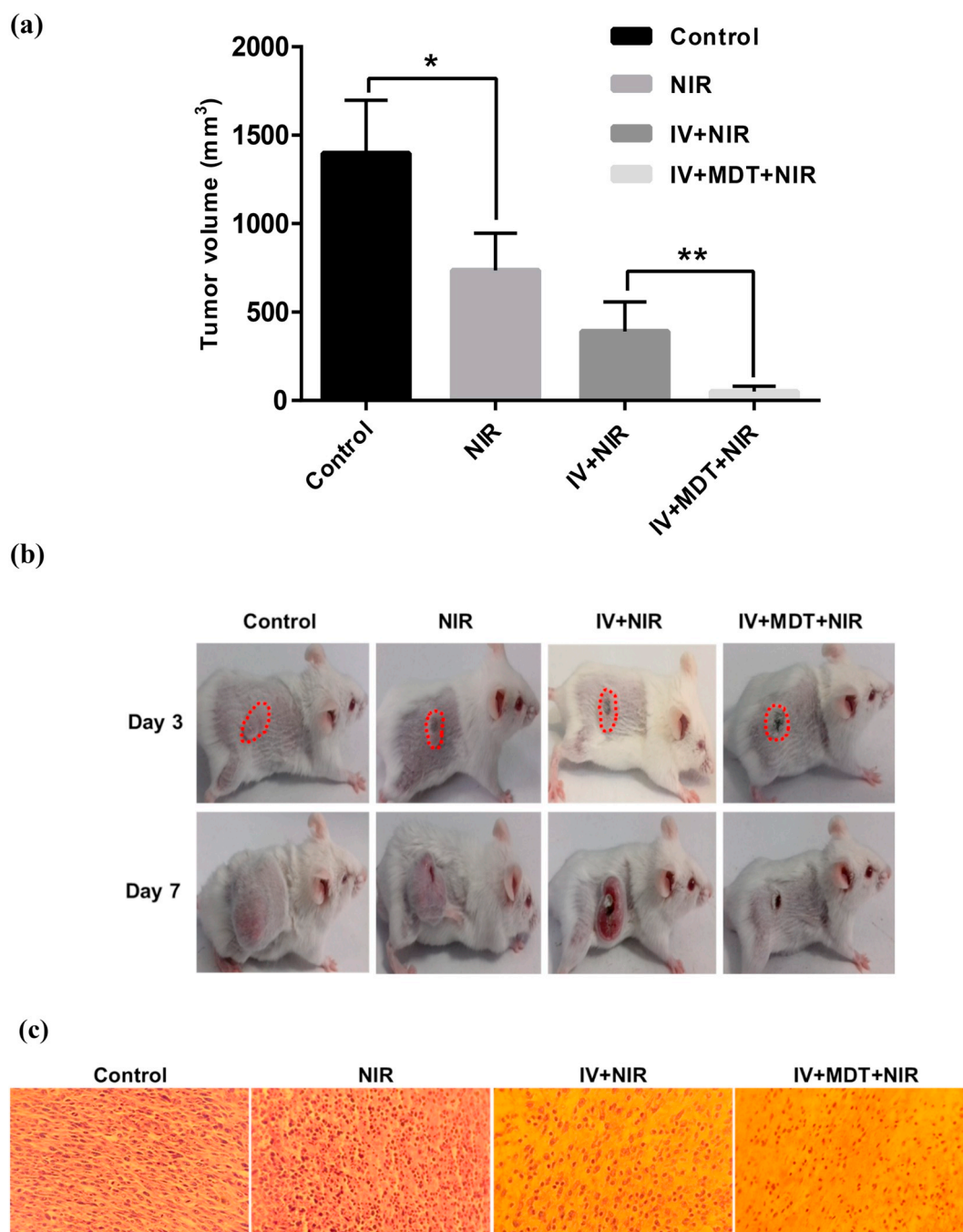
(a)

(b)

(c)

Fig. 6. In vivo antitumor effect of NPTT using IO@Au nanoparticles. (a) Tumor volume and (b) representative photographs of CT26 tumor-bearing mice, 3 and 7 days post-treatment. (c) Histological features of tumor tissue harvested from mice 48 h post-treatment by H&E staining. (* P value < .05, ** P value < .001). The difference in tumor volume between NIR and IV + NIR was not significant.

geometry and nanoparticles localization would be a great step toward improving the accuracy and prediction power of heat transfer simulation. Due to magnetic and light-responsive properties, IO@Au can be utilized as both NPTT and MRI contrast agents at the same time. Accordingly, in the present study, the tumor geometry and nanoparticles localization were obtained from MR image of tumor-bearing mice and used for theoretical calculations of heat transfer process.

A homogeneous distribution of nanoparticles is required to achieve temperature uniformity throughout the tumor volume. Unfortunately, as evidenced from the MRI studies (Fig. 2) the nanoparticle distribution is rather heterogeneous suggesting that only small regions of the tumor will be susceptible to NPTT-mediated destruction and hence, tumor

cure cannot be achieved. The data in Fig. 6 support this as it shows no statistically significant difference in tumor volumes between NIR and NIR + IV groups. A statistically significant difference in efficacy is however observed using the targeted approach (IV + MDT + NIR). This is an important observation since it suggests that, in agreement with the findings of many other studies, passive targeting of nanoparticles to tumors is ineffective and that active targeting approaches are required to achieve sufficient concentrations of nanoparticles in the tumor.

Although the findings of this study show that magnetic fields can be employed to target nanoparticles to tumors, the particles are clustered near the tumor surface which may limit temperature increases to the superficial regions leaving the deeper tumor volumes untreated. This

suggests that a more efficient nanoparticle administration route is required in order to achieve a uniform distribution of nanoparticles throughout the entire tumor volume.

5. Conclusion

The purpose of this study was to establish a numerical modeling method for prediction of temperature distribution during NPTT. Utilizing the realistic tumor geometry and nanoparticle distribution is essential to enhance the prediction power of heat transfer modeling. Accordingly, we exploited the theranostic potential of IO@Au nanoparticles to enable NPTT under NIR laser irradiation while their spatial location can be traced via MRI. The geometrical model description of tumor with the corresponding nanoparticle distribution map provided by MRI were used for finite element simulation of heat transfer process. The constructed model has the potential to be used as an individualized pre-treatment planning approach in order to improve the heat delivery to the tumor by modifying the treatment parameters before the actual heating operation.

Declaration of Competing Interest

Nothing to be declared.

Acknowledgments

References

[1] M. Hurwitz, P. Stauffer, Hyperthermia, radiation and chemotherapy: The role of heat in multidisciplinary cancer care, Seminars in Oncology, Elsevier, 2014, pp. 714–729.

[2] J. Beik, M. Khateri, Z. Khosravi, S.K. Kamrava, S. Kooranifar, H. Ghaznavi, A. Shakeri-Zadeh, Gold nanoparticles in combinatorial cancer therapy strategies, Coord. Chem. Rev. 387 (2019) 299–324.

[3] M. Raoof, B.T. Cisneros, S.J. Corr, F. Palalon, S.A. Curley, N.V. Koshkina, Tumor selective hyperthermia induced by short-wave capacitively-coupled RF electric-fields, PLoS ONE 8 (2013) e68506.

[4] J. Beik, M.B. Shiran, Z. Abed, I. Shiri, A. Ghadimi-Daresajini, F. Farkhondeh, H. Ghaznavi, A. Shakeri-Zadeh, Gold nanoparticle-induced sonosensitization enhances the antitumor activity of ultrasound in colon tumor-bearing mice, Med. Phys. 45 (2018) 4306–4314.

[5] M. Mirrahimi, Z. Abed, J. Beik, I. Shiri, A.S. Dezfuli, V.P. Mahabadi, S.K. Kamrava, H. Ghaznavi, A. Shakeri-Zadeh, A thermo-responsive alginate nanogel platform co-loaded with gold nanoparticles and cisplatin for combined cancer chemo-photothermal therapy, Pharmacol. Res. 143 (2019) 178–185.

[6] Z. Abed, J. Beik, S. Laurent, N. Eslahi, T. Khani, E.S. Davani, H. Ghaznavi, A. Shakeri-Zadeh, Iron oxide–gold core–shell nano-theranostic for magnetically targeted photothermal therapy under magnetic resonance imaging guidance, J. Cancer Res. Clin. Oncol. 145 (2019) 1213–1219.

[7] Z. Alamzadeh, J. Beik, V.P. Mahabadi, A.A. Ardekani, A. Ghader, S.K. Kamrava, A.S. Dezfuli, H. Ghaznavi, A. Shakeri-Zadeh, Ultrastructural and optical characteristics of cancer cells treated by a nanotechnology based chemo-photothermal therapy method, J. Photochem. Photobiol. B Biol. 192 (2019) 19–25.

[8] M. Mirrahimi, M. Khateri, J. Beik, F.S. Ghoreishi, A.S. Dezfuli, H. Ghaznavi, A. Shakeri-Zadeh, Enhancement of chemoradiation by co-incorporation of gold nanoparticles and cisplatin into alginate hydrogel, J Biomed Mater Res Part B. (2019) 1–6.

[9] J. Mesicek, K. Kuca, Summary of numerical analyses for therapeutic uses of laser-activated gold nanoparticles, Int. J. Hyperth. (2018) 1–10.

[10] M.W. Dewhirst, J. Abraham, B. Viglianti, Evolution of thermal dosimetry for application of hyperthermia to treat cancer, Advances in Heat Transfer, Elsevier, 2015, pp. 397–421.

[11] M. Keshavarz, K. Moloudi, R. Paydar, Z. Abed, J. Beik, H. Ghaznavi, A. Shakeri-Zadeh, Alginate hydrogel co-loaded with cisplatin and gold nanoparticles for computed tomography image-guided chemotherapy, J. Biomater. Appl. 33 (2) (2018) 161–169.

[12] J. Beik, M. Jafariyan, A. Montazerabadi, A. Ghadimi-Daresajini, P. Tarighi, A. Mahmoudabadi, H. Ghaznavi, A. Shakeri-Zadeh, The benefits of folic acid-modified gold nanoparticles in CT-based molecular imaging: radiation dose reduction and image contrast enhancement, Artif. Cells Nanomed. Biotechnol. 46 (2018) 1993–2001.

[13] N. Eyvazzadeh, A. Shakeri-Zadeh, R. Fekrazad, E. Amini, H. Ghaznavi, S.K. Kamrava, Gold-coated magnetic nanoparticle as a nanotheranostic agent for magnetic resonance imaging and photothermal therapy of cancer, Lasers Med. Sci. 32 (2017) 1469–1477.

[14] H. Ghaznavi, S. Hosseini-Nami, S.K. Kamrava, R. Irajirad, S. Maleki, A. Shakeri-Zadeh, A. Montazerabadi, Folic acid conjugated PEG coated gold–iron oxide core–shell nanocomplex as a potential agent for targeted photothermal therapy of cancer, Artif. Cells Nanomed. Biotechnol. 46 (2018) 1594–1604.

[15] Z. Qin, J.C. Bischof, Thermophysical and biological responses of gold nanoparticle laser heating, Chem. Soc. Rev. 41 (2012) 1191–1217.

[16] M. Mirrahimi, V. Hosseini, S.K. Kamrava, N. Attaran, J. Beik, S. Kooranifar, H. Ghaznavi, A. Shakeri-Zadeh, Selective heat generation in cancer cells using a combination of 808 nm laser irradiation and the folate-conjugated Fe2O3@ Au nanocomplex, Artif. Cells Nanomed. Biotechnol. 46 (2018) 241–253.

[17] U. Topaloglu, Y. Yan, P. Novak, P. Spring, J. Suen, G. Shafirstein, Virtual thermal ablation in the head and neck using Comsol MultiPhysics, Proceedings of the COMSOL Conference, 2008, pp. 1–7.

[18] M.N. Iizuka, I.A. Vitkin, M.C. Kolios, M.D. Sherar, The effects of dynamic optical properties during interstitial laser photocoagulation, Phys. Med. Biol. 45 (2000) 1335.

[19] S.K. Cheong, S. Krishnan, S.H. Cho, Modeling of plasmonic heating from individual gold nanoshells for near-infrared laser-induced thermal therapy, Med. Phys. 36 (2009) 4664–4671.

[20] N. Manuchehrabadi, L. Zhu, Gold nanoparticle-based laser photothermal therapy, Handbook of Thermal Science and Engineering, 2017, pp. 1–33.

[21] Y. Ren, H. Qi, Q. Chen, L. Ruan, Thermal dosage investigation for optimal temperature distribution in gold nanoparticle enhanced photothermal therapy, Int. J. Heat Mass Transf. 106 (2017) 212–221.

[22] Y. Feng, M. Rylander, J. Bass, J. Oden, K. Diller, Optimal design of laser surgery for cancer treatment through nanoparticle-mediated hyperthermia therapy, NSTI-Nanotech, 2005, pp. 39–42.

[23] H.H. Pennes, Analysis of tissue and arterial blood temperatures in the resting human forearm, J. Appl. Physiol. 1 (1948) 93–122.

[24] S. Soni, H. Tyagi, R.A. Taylor, A. Kumar, Experimental and numerical investigation of heat confinement during nanoparticle-assisted thermal therapy, Int. Commun. Heat Mass Tran. 69 (2015) 11–17.

[25] A.R. Melo, M.M.S. Loureiro, F. Loureiro, Blood perfusion parameter estimation in Tumors by means of a genetic algorithm, Procedia Comput. Sci. 108 (2017) 1384–1393.

[26] J. van der Zee, Heating the patient: a promising approach? Ann. Oncol. 13 (2002) 1173–1184.

[27] J. van der Zee, J.N. Peer-Valstar, P.J. Rietveld, L. de Graaf-Strukowska, G.C. van Rhoon, Practical limitations of interstitial thermometry during deep hyperthermia, Int. J. Radiat. Oncol. Biol. Phys. 40 (1998) 1205–1212.

[28] G.C. Van Rhoon, P. Wust, Introduction: non-invasive thermometry for thermotherapy, Int. J. Hyperth. 21 (2005) 489–495.

[29] N. Manuchehrabadi, L. Zhu, Development of a computational simulation tool to design a protocol for treating prostate tumours using transurethral laser photothermal therapy, Int. J. Hyperth. 30 (2014) 349–361.

[30] J. Wiersma, J. Van Dijk, RF hyperthermia array modelling; validation by means of measured EM-field distributions, Int. J. Hyperth. 17 (2001) 63–81.

[31] P. Wust, R. Beck, J. Berger, H. Fähling, M. Seebass, W. Wlodarczyk, W. Hoffmann, J. Nadobny, Electric field distributions in a phased-array applicator with 12 channels: measurements and numerical simulations, Med. Phys. 27 (2000) 2565–2579.

[32] A. LeBrun, R. Ma, L. Zhu, MicroCT image based simulation to design heating protocols in magnetic nanoparticle hyperthermia for cancer treatment, J. Therm. Biol. 62 (2016) 129–137.

[33] Y.-G. Lv, Z.-S. Deng, J. Liu, 3-D numerical study on the induced heating effects of embedded micro/nanoparticles on human body subject to external medical electromagnetic field, IEEE Trans. Nanobiosci. 4 (2005) 284–294.

[34] M. Salloum, R. Ma, L. Zhu, An in-vivo experimental study of temperature elevations in animal tissue during magnetic nanoparticle hyperthermia, Int. J. Hyperth. 24 (2008) 589–601.